ORIGINAL CONTRIBUTION

Alexandre Ioan Romoscanu
Mahir Behar Sayir
Klaus Häusler
Adam Stewart Burbidge

High frequency parallel plate probe for the measurement of the complex viscosity of liquids

A.I. Romoscanu (✉) · M.B. Sayir
K. Häusler
Institute of Mechanics,
Swiss Federal Institute of Technology,
8092 Zurich, Switzerland
E-mail: romoscanu@imes.mavt.ethz.ch

A.S. Burbidge
Nestlé Research Center,
Vers-chez-les-Blanc,
26 Lausanne, Switzerland

Abstract In this work an instrument is described which measures the complex shear viscosity of liquids in the kHz frequency range. The instrument is driven electromagnetically and operates in resonant mode. The measurement of the primary data, from which the rheological properties of the fluid sample are inferred, does not include any deflection amplitude measuring step and is purely digital. Models allowing the interpretation of the probe primary data in terms of fluid complex viscosity are presented. The theoretically predicted mechanical behaviour of the probe is compared with the measured one and the rheometric ability of the device is discussed.

Keywords Rheometry · Linear viscoelasticity · Complex shear viscosity · Resonance · Resonator · High frequency · Damping

Introduction

In this work, we explore the application of oscillating probes as a measuring device for the rheological properties of fluid films. Our goal is to develop an essentially simple and reliable instrument capable of measuring the complex viscosity of fluids in the kHz frequency range, which is usually inaccessible to classical rheometers. At such frequencies, the instrument own contribution to the dynamical behaviour of the system instrument + fluid begins to be very important, and this contribution is usually difficult to model for conventional instruments involving macroscopically moving parts. Hence, the method used here is precisely based on the simplicity of the sensing device and the consequent predictability of its dynamical behaviour at resonance.

The instrument described in this work is not the first attempt to investigate the rheological properties of fluids at frequencies which are unreachable for instruments with macroscopically moving parts. A review of high

frequency measuring methods is given for instance in Stokich et al. (1994) where an instrument working in torsional free decay is also described. Among these, one can mention the pioneering work of Mason (1947) who derived a relationship between the dynamic behaviour of an oscillator in the vicinity of its resonance frequency and the sample rheological properties which has been used in many works published since then. The multiple lump resonator (MLR), first suggested by Birnboim and Elyash (1966) and developed by Schrag and Johnson (1971), the magnetostrictive instrument of Glover et al. (1968), the torsion pendulum described by Blom and Mellema (1984) or the recent piezoelectrically-driven, non-resonant instrument proposed by Kirschenmann and Pechhold (2002) can also be mentioned in this non-exhaustive list.

An essential difference between these instruments and the one presented in this work is the fact that no amplitude or resonance bandwidths are measured here. The method relies entirely on the digital measurement of the phase shift between a periodic driving force and the

damped harmonic deflection of a monolithic structure in the vicinity of its resonant frequency. The fact that no amplitude measurements are performed eliminates the accuracy loss linked with an analogical deflection amplitude measuring step, and helps reduce the cost of the instrument. Operation in the vicinity of the resonant frequency allows sufficiently large deflection amplitudes and thus fluid strains to be reached with a relatively robust structure at minimal driving force, thus allowing the resonator to be driven electromagnetically instead of, for instance, piezoelectrically. Further, the measurement method makes use of one single electromagnetic driving and sensing device, in the sense that one coil/magnet combination plays the roles of both actuator and sensor, in a successive manner. This efficiently eliminates disturbing cross-talk between sensor and actuator, although the measurement is not anymore a strictly stationary one, since driving periods are interrupted by sensing ones. The effects of the successive driving and sensing method (further referred to as *pseudo-stationary*) are briefly outlined below; a more detailed discussion can be found in Romoscanu (2003). Truly stationary measurements are also made for comparison, with the help of a function generator and a laser interferometer. A further feature of the device presented here is the calibration-free, modelled approach, which is made possible by the simple geometry. This contrasts with a feature shared by many commercially available devices, which is a calibration-based conversion of the measured damping into the fluid viscosity. The main disadvantage of a calibrated approach is that identification of the steady shear or low-frequency reference viscosity with the viscosity of the fluid at the essentially higher instrument frequency is not justified for fluids with relaxation times of a similar order of magnitude than the reciprocal instrument frequency. As shown for instance by Hadjistamov (1996), the range of Newtonian PDMS melts is strongly limited when the measuring frequency is in the kHz range or higher.
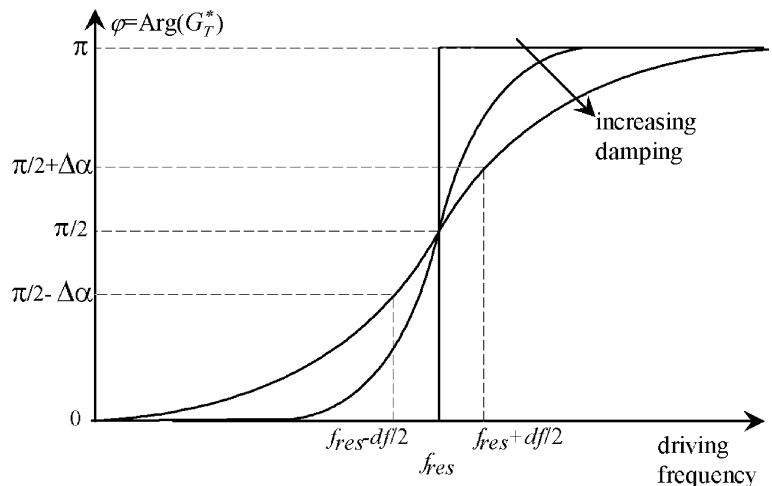
In the present work, we derive the mechanical behaviour of the system directly from the equations of motion and constitutive equations of both resonator and fluid. Basically, this allows the integration of arbitrary fluid constitutive equations provided that a solution is found to the equation of motion of the fluid with the respective fluid constitutive equation. We limit ourselves to linear constitutive equations. Sample inertia is taken into account for measurements on low viscous fluids are not necessarily performed at low Reynolds number.

Measurement principle

From a mechanical point of view, the viscosity of a fluid quantifies the amount of energy which is dissipated per unit time when the fluid experiences shearing. When brought into contact with an oscillator in such a way that the oscillator deformation induces a shear flow, the fluid viscosity effectively acts as an additional damping source for the oscillator. The dynamical behaviour of such a damped oscillator can thus be used to quantify the viscosity, with a precision which is directly linked to the degree and quantitative knowledge of other sources of damping, such as intrinsic material damping. When the dynamical behaviour is quantified with two independent quantities, viscosity and elasticity, i.e. the complex viscosity η^* can in principle be measured. The sensitivity of the probe and the accordance between theory and measurements determine whether the oscillator can be used as a reliable rheometric device or not.

Practically, the dynamical behaviour of the system consisting of the resonating oscillator and damping fluid is quantified with two values: the damping df, which quantifies the slope of the curve which represents the phase shift between driving force and measured deflection vs driving frequency, at the resonant frequency, as well as the resonant frequency f_{res} itself.

Fig. 1 Phase shift $\phi = \text{Arg}(G_T^*)$ vs driving frequency f

The phase shift $\phi(f)$ in the vicinity of f_{res} for a typical resonator is plotted in Fig. 1 for increasing damping. $\phi(f)$ corresponds to the argument of the system transfer function

$$G_T^*(f) = \frac{\widehat{F}}{\widehat{X}} \qquad (1)$$

which is the complex ratio between $\widehat{F}$, the complex amplitude of the harmonic force $F(t) = \widehat{F}e^{i\omega t}$ exerted on the oscillator and $\widehat{X}$, the complex amplitude of the harmonic deflection function $X(t) = \widehat{X}e^{i\omega t}$. For an ideally elastic resonator with no damping, the transition of $\phi(f)$ from 0 to π has the shape of a step function located in $f = f_{res}$. Under the effect of the damping this slope is reduced from infinity to finite values. We quantify this slope with the frequency difference df corresponding to a phase shift difference of $2\Delta\alpha$ centred in $\phi = \pi/2$. $\Delta\alpha$, f_{res} and df, also plotted in Fig. 1, are mathematically defined with

$$\varphi(f_{res}) = \mathrm{Arg}(G_T * (f_{res})) = \pi/2, \qquad (2)$$

$$\varphi(f_{res} \pm df/2) = \mathrm{Arg}(G_T * (f_{res} \pm df/2)) = \pi/2 \pm \Delta\alpha. \qquad (3)$$

For $\Delta\alpha \leq \pi/4$, df is a sufficiently precise measure of the slope of $\phi(f)$ around f_{res}, i.e.

$$\left.\frac{\partial\varphi(f)}{\partial f}\right|_{f=f_{res}} \cong \frac{2\Delta\alpha}{df} \qquad (4)$$

In the present arrangement, f_{res} and df are obtained with the algorithm outlined in Fig. 2. A full description of the electronic circuit is given in Sayir et al. (1995). Basically, a periodic square tension signal is produced by a voltage controlled power amplified function generator (VCO). This signal is simultaneously fed to a coil which electromagnetically drives the resonator as well as to a phase shifter (PS), which alternatively shifts the signal by a fixed angle $\pi/2 \pm \Delta\alpha$. After a given number n_D of driving cycles (between 3 and 12 in the present arrangement), the electromagnetic actuator turns into a sensor, for the remaining $(15 - n_D)$ cycles. During this sensing period, the phase difference between the sensed deflection si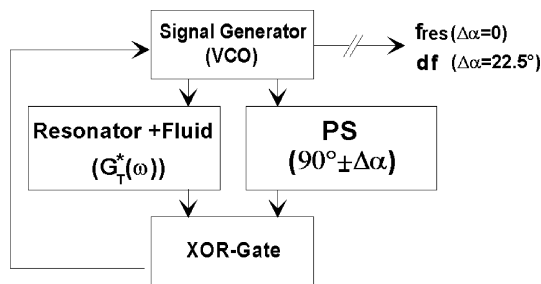gnal and the $\pi/2 \pm \Delta\alpha$ PS-shifted driving signal is measured with the help of an XOR-gate. The gate is linked to a PI-regulator which transforms the XOR-gate signal into a tension increment, which is used to correct the frequency of the VCO function generator. This results in a phase-locked loop, for the driving frequency is continuously adjusted until sensed and PS-shifted signals are in phase, and the PI correcting tension vanishes. Finally, the difference df and the average of the driving frequencies corresponding to both phase shifts $\pi/2 \pm \Delta\alpha$ are computed. Their average over a given period of time, usually set to 1 s, is recorded with a PC via an RS232 connection. The resonant frequency itself is the average of these frequencies, and corresponds to the frequency which the phase locked loop reaches with $\Delta\alpha$ set to 0 Hz.

The measured values f_{res} and df are a measure of the elastic and viscous characters of the oscillator and fluid system. Provided the probe characteristics and fluid density are known, these two independent values can be linked to two independent fluid properties, like the real and imaginary part of the complex viscosity $\eta^* = \eta' - i\eta''$.

It is important to note that with the above described measuring method, the sensitivity for the measurement of viscosity is intrinsically better than the sensitivity for the measurement of elasticity. One reason is the relatively low contribution of the fluid elasticity to the total stiffness of a system partially composed of a monolithic highly elastic resonator. In contrast, the relative contribution of the fluid to the total damping is essentially higher. Elasticity is also measured from an f_{res} shift, and not from the absolute f_{res} value, unlike df which is an absolute measure of the system total damping. Finally, with the algorithm described above, f_{res} is located from the theoretical symmetry of the $\phi(f)$ curve in the vicinity f_{res}, in absence of any amplitude measurement.

In the following section, we obtain expressions for f_{res} and df as functions of η' and η''. As will be shown, the accuracy of the phase-shift based detection system allows viscosity as well as elasticity measurements to be made, provided some conditions are fulfilled.

System modelling

The determination of the mechanical properties of the fluid sample from the primary data f_{res} and df requires knowledge of the complex transfer function $G_T^*(f)$ of the coupled oscillator and fluid system, following Eqs. (2) and (3) above. We describe hereafter the resonator geometry, compute the stress resulting from shearing the fluid sample and outline two possible ways to derive the system transfer function $G_T^*(f)$.

Geometry

In the present geometry, a fluid film is confined between a fixed plate and a resonating structure whose

Fig. 2 Phase-locked loop algorithm for the amplitude-free measurement of the system damping

deformation induces a plane shear flow in the fluid. The fixed and oscillating plates are parallel at all times, the moving one oscillating nearly exactly in its plane. The thickness d of the fluid sample can be adjusted and is an important parameter for the dynamical behaviour of the system. The confined fluid geometry has two advantages over other possible geometries like torsionally oscillating rods or tubes, where the fluid is a semi-infinite medium. First, the two boundary conditions which are imposed to the velocity field induce an increased sensitivity, especially in the high viscosity range, as shown below. Second, the effect of confinement on the rheological properties of the sample can be investigated. A sketch of the oscillator geometry illustrating the parameters used in the models proposed below is shown in Fig. 3a, together with the parallel spring setup which allows the adjustment of the gap width d. A picture of the assembled instrument, together with the mirrors used to verify the parallelism of the plates as well as the quantity of confined fluid is shown in Fig. 3b.

Flow

We derive here the shear force exerted by the shear fluid on the oscillating plate. The equation of motion in x-direction is (Bird et al. 1987)

$$\rho \frac{\partial v_x}{\partial t} = -\frac{\partial \tau_{yx}}{\partial y} \tag{5}$$

We shall limit ourselves here to the consideration of linear flows. The general constitutive equation for the linear viscoelastic fluid is (Tanner 2000)

$$\tau_{yx} = -\int_{-\infty}^{t} G(t-t') \frac{\partial v_x(y,t')}{\partial y} dt' \tag{6}$$

so that the differential equation for the velocity field in the gap $v_x(y,t)$ reads

$$\rho \frac{\partial v_x}{\partial t} = \int_{-\infty}^{t} G(t-t') \frac{\partial^2 v_x(y,t')}{\partial y^2} dt' \tag{7}$$

Since the fluid is linear, we expect the velocity field to oscillate harmonically in time and have a y-dependent amplitude and phase lag once all transients have died out. Substitution of

$$v_x(y,t) = \widehat{V}(y) e^{i\omega t} \tag{8}$$

in Eq. (7) yields

$$\rho i\omega \widehat{V}(y) = \frac{\partial^2 \widehat{V}(y)}{\partial y^2} \int_{-\infty}^{t} G(t-t') e^{i\omega(t'-t)} dt'$$
$$= \frac{\partial^2 \widehat{V}(y)}{\partial y^2} \int_{0}^{\infty} G(s) e^{-i\omega s} ds \tag{9}$$

with $s = t - t'$. With the following definition of the complex viscosity η^* (Tanner 2000),

$$\eta^* = \eta' - i\eta'' = \int_{0}^{\infty} G(s) e^{-i\omega s} ds \tag{10}$$

we need to solve

$$\frac{\rho i \omega}{\eta^*} \widehat{V}(y) = \frac{\partial^2 \widehat{V}(y)}{\partial y^2} \tag{11}$$

This is the same equation as the one which arises in the particular Newtonian case. The BC for the y-dependent complex velocity amplitude $\widehat{V}(y)$ of the fluid confined between the oscillating and fixed plates are

$$\widehat{V}(0) = i\omega \widehat{X}, \tag{12}$$

$$\widehat{V}(d) = 0. \tag{13}$$

The solution of Eq. (11) with these BC reads

$$\widehat{V}(y) = i\omega \widehat{X} \frac{\mathrm{Sinh}\left(\frac{d-y}{\delta}\sqrt{2i}\right)}{\mathrm{Sinh}\left(\frac{d}{\delta}\sqrt{2i}\right)} \tag{14}$$

where δ is given by

$$\delta = \sqrt{\frac{2\eta^*}{\omega\rho}}. \tag{15}$$

$|\delta|$ is of the same order of magnitude as the penetration depth of the shear wave in a semi-infinite medium (Landau and Lifshitz 1994). δ and the gap Reynolds number Re are linked with

$$Re = 2\left(\frac{d}{\delta}\right)^2. \tag{16}$$

The complex amplitude of the harmonic shear stress exerted by the fluid on the plate is given by

$$\widehat{\tau}_{yx} = \eta^* \frac{\partial \widehat{V}(y)}{\partial y}\bigg|_{y=0} = -\widehat{X}\sqrt{i\eta^*\omega^3\rho}\,\mathrm{Coth}\left(\sqrt{iRe}\right) \tag{17}$$

Equation (17) shows the positive influence of the finite sample thickness d on the probe sensitivity in the higher viscosity range. While in the high Re limit ($d >> \delta$ or semi-infinite sample geometry) the hyperbolic cotangent tends to 1 and thus $|\widehat{\tau}_{yx}| \sim |\eta^*|^{1/2}$, at low Re the hyperbolic cotangent scales with $|\eta^*|^{1/2}$, i.e. $|\widehat{\tau}_{yx}| \sim |\eta^*|$.

Resonator

The monolithic resonator used in this work consists of two supporting walls and one translating plate, whose upper side is in contact with the fluid, which is in turn bounded by another fixed plate in distance d as well as its own surface tension. The resonator is made of titanium using an electro erosion method; resonator dimensions are given in Table 1. A coil/magnet combination exerts an oscillating force on the upper

Fig. 3a Parallel plate probe
geometry: (1) 6.0 mm micro-
metric screw for the adjustment
of *d*; (2) parallel springs; (3)
upper, fixed polished glass
plate; (4) lower, oscillating
polished glass plate; (5) driving
coil; (6) magnet; (7) thin,
compliant part of the lateral
walls; (8) thick, rigid part of the
lateral walls. **b** Parallel plate
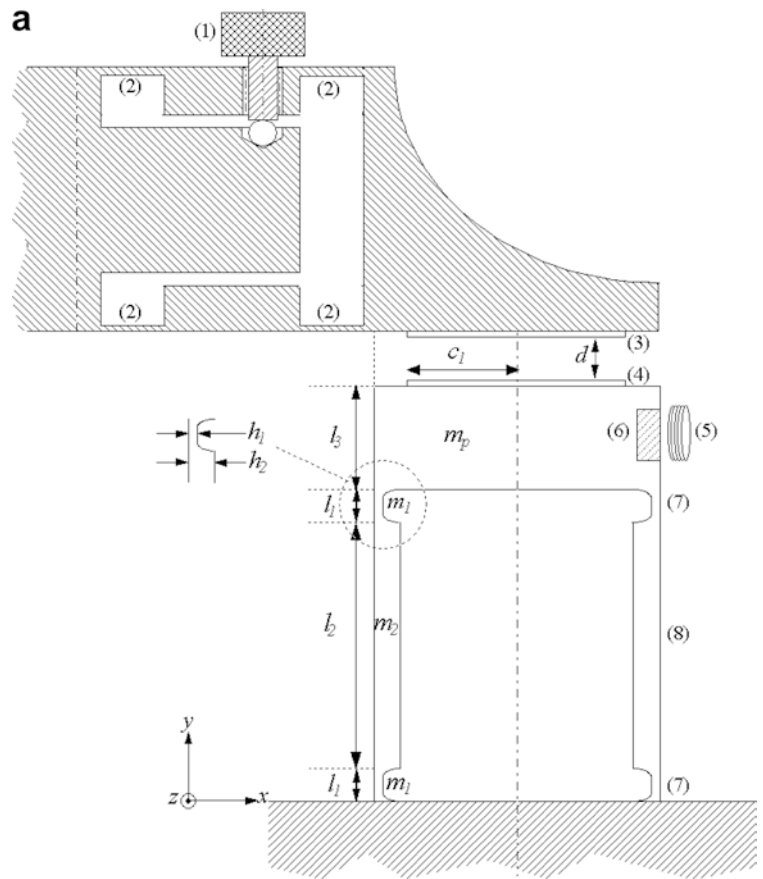probe: assembled instrument

Table 1 Resonator parameters

Parameter	Description	Value for discrete model	Value for continuous model
E/Pa	Resonator tensile complex modulus	$101.2{\times}10^9 + 7{\times}10^7 i$	
$\rho_{resonator}$/kg·m^{-3}	Resonator density	4500	
m_p/g	Mass of rigid oscillating plate	7.92	
m_s/kg	Mass of upper and lower lateral wall parts	1.50	
m_2/g	Mass of central lateral wall part	0.132	
l_1/mm	Length of upper and lower lateral wall parts	4.2	3.2
l_2/mm	Length of central lateral wall part	$24.0 - l_1$/mm	
l_3/mm	Distance between top of lateral wall and fluid	8.0	–
h_1/mm	Thickness of upper and lower lateral wall parts	0.83	
h_2/mm	Thickness of central lateral wall part	2.0	
c_1/mm	Half distance between lateral walls	10.6	–
c_2/mm	Resonator depth	10.0	
ΔS/mm^2	Surface in contact with fluid	150.0	
ρ_{fluid}/kg·m^{-3}	Fluid density	1000	

plate in the x direction in such a way that the plate oscillates laterally with minimal vertical motion. Keeping the vertical deflection minimal is essential in order to minimize additional acoustic damping of the system. If we define α as the lateral deflection angle of the structure, the ratio of vertical to lateral deflection amplitudes is of O($\alpha/2$). With typical α values of O(10^{-3}), the ratio of vertical to horizontal deflection is of O(10^{-3}) i.e. acoustic loss is quantitatively negligible.

The resonator can be modelled either as a discrete oscillator or as a continuously deformable structure. Both approaches imply an idealization to some extent of the actual structure. The discrete approach is based on the assumption that the total compliance is mainly concentrated in a limited number of points, and consequently the remaining parts of the structure describe rigid body motions. While this approach is mathematically more convenient, it will lose in validity the larger the deformable segments are, and will only predict one fundamental frequency, which corresponds to the only possible deformation allowed by point-like springs. On the other hand, the continuous approach is able to predict higher fundamental frequencies, but is practically much less convenient to use, especially since the resonator + fluid system model has to be finally inverted in order to compute the viscosity from measured dynamical behaviour. In the following we outline the discrete and continuous models of the resonator and confront the theoretical dynamical behaviours around the first fundamental frequency given by both models before comparing them with measured values.

Discrete model

In a discrete approach, deformation occurs mainly the in four thinner parts of both lateral walls with height l_1. The concentration of the deformation in these four flexion springs is based on the fact that in a linear

approach flexion compliance scales linearly with the inverse of the flexion moment I_z, which is linked to c, the width, and h, the thickness of the considered cross section by

$$I_z = \frac{c\,h^3}{12}. \tag{18}$$

Since the thickness of the springs is about one-third of the thickness of the lateral walls, the springs are ca. 30 times more compliant than the thicker central part of the lateral walls.

Since the system is statically over-determined, we separate virtually the structure in three parts, namely the two lateral walls including the springs, and the upper plate. We represent each of these elastic junctions as well as the points where the resonator is fixed to the ground by one lateral force F_i in the x direction, one normal force N_i in the y direction as well as a flexion moment M_i in the z direction, where i refers to the ith compliant junction out of four. In order to include the "spring length" l_1 explicitly in our model, we first derive an expression for the flexion moment M in the z direction in the form of a proportionality constant κ between moment and lateral deflection ξ in $y = 2l_1 + l_2 + l_3$, i.e. $M = \kappa\xi$. The solution of the above geometry under a constant deflection ξ of the upper plate the x direction yields a proportionality constant

$$\kappa = \frac{3EI_Z(2l_1 + l_2)}{l_1\left(4l_1^2 + 6l_1 l_2 + 3l_2^2\right)}. \tag{19}$$

With this formalism, we have 13 unknown values, namely two forces and one moment in each of the 4 junctions, plus the lateral deflection amplitude of the upper plate $\bar{X}$. The 13 equations of this linear system (three for each rigid part of the resonator, plus four which link the spring moments with the deflection $\bar{X}$) are:

– Upper plate (Newton's law in the x respectively y directions, and total moment in the z direction):

$$\Delta S \widehat{\tau}_{yx} - F_1 - F_2 + \widehat{F} = -m_p \omega^2 \widehat{X} \tag{20}$$

$$N_1 + N_2 - m_p \, g = 0 \tag{21}$$

$$(F_1 + F_2)\frac{l_3}{2} + \Delta S \frac{l_3}{2}\widehat{\tau}_{yx} + c_1 N_1 - c_1 N_2 + M_1 + M_2 = 0 \tag{22}$$

transfer function, Eq. (31). The values of df and f_{res} as functions of the fluid complex viscosity η^* are found by solving Eqs. (2) and (3) above, with Newton's or secant method.

$$I_i = \frac{m_i}{12}\left(l_i^2 + h_i^2\right) \tag{30}$$

$$G_T^*(\omega) = \omega^2 \frac{m_2 m_1 (l_1 + l_2)^2 + 4 I_2(m_2 + m_s) + 4 I_1(m_2 + m_1) - (l_1 m_1 + l_2(m_2 + 2m_1))^2}{2(l_1 + l_2)^2 (m_2 + m_1)}$$
$$- \omega^{3/2}\left(m_p\sqrt{\omega} - \Delta S \sqrt{i\eta^*\rho}\,\mathrm{Coth}\left(d\sqrt{\frac{i\omega\rho}{\eta^*}}\right)\right) + \frac{8\kappa}{2(l_1 + l_2)} \tag{31}$$

– Left-hand lateral wall (Newton's law in x resp. y directions, and total moment in z direction):

$$F_1 - F_4 = -\left(\frac{m_2 l_2 + m_1(2l_2 + l_1)}{2(l_2 + l_1)}\right)\omega^2\widehat{X} \tag{23}$$

$$N_4 - N_1 - (m_2 + m_1)g = 0 \tag{24}$$

$$\omega^2\widehat{X}\frac{(l_1 + l_2)m_2 m_1 + 4I_2(m_2 + m_1) + 4I_1(m_2 + m_1)}{4(m_2 + m_1)(l_1 + l_2)}$$
$$+ \left((l_2 + l_1) - \left(\frac{m_2 l_2 + m_1(2l_2 + l_1)}{2(m_2 + m_1)}\right)\right)F_1$$
$$+ \left(\frac{m_2 l_2 + m_1(2l_2 + l_1)}{2(m_2 + m_1)}\right)F_4 - M_1 + M_4 = 0 \tag{25}$$

– Right-hand lateral wall (analogy equations, Newton's law in y-direction):

$$F_1 = F_2 \tag{26}$$

$$F_3 = F_4 \tag{27}$$

$$N_3 - N_2 - (m_2 + m_1)g = 0 \tag{28}$$

– Springs:

$$M_1 = M_2 = M_3 = M_4 = \kappa\widehat{X} \tag{29}$$

In Eq. (25) we have neglected the contribution of the normal forces N_i to the moment in z-direction basing on the small deflection. The parameters I_i denote the rotation inertial moments along the z-axis of the flexible and rigid parts respectively to their centre of gravity. They are defined with Eq. (30) (Sayir 1994) where m_i, h_i and l_i are respectively the mass, the thickness and the height of the ith segment. Substitution of the solution for $\widehat{X}$ of the above equation system in Eq. (1) yields the system's

Continuous model

We suppose that the lateral walls of the resonator exert flexural oscillations under the dynamic loading the of the driving magnet and sheared fluid. In the present structure, each wall consists of three parts with same width but different length and cross section. For simplification reasons, we consider the case where the lower and uppermost parts have same length and thickness l_1 and h_1.

Assuming a linear elastic material behaviour, small deformations as well as "thin" walls, defined by

$$\frac{h}{\lambda} \ll 1 \tag{32}$$

where λ is the wave length of the flexural oscillation and h the structure thickness, the differential equation which governs flexural oscillations reads

$$\rho A \frac{\partial^2 u}{\partial t^2} + E I_z \frac{\partial^4 u}{\partial y^4} = 0 \tag{33}$$

where u is the transversal deflection in x-direction, y the coordinate along the deformable wall, A the local cross section of the structure, ρ its density and I_z the flexural inertial moment, Eq. (18). Assuming a harmonic deflection $u(y,t) = u(y)e^{i\omega t}$, Eq. (33) becomes the ODE

$$-k^4 u(y) + \frac{\partial^4 u(x)}{\partial y^4} = 0 \tag{34}$$

with

$$k^4 = \frac{\omega^2 \rho A}{E I_z}. \tag{35}$$

The general solution of Eq. (34) reads

$$u(x) = c_1 e^{-kx} + c_2 e^{-kx} + c_3 \cos(kx) + c_4 \sin(kx). \tag{36}$$

The deflection function of each lateral wall consists of three such functions defined over $[0, l_1]$, $[l_1, l_1 + l_2]$ and $[l_1 + l_2, 2l_1 + l_2]$, which in the following are referred to as

segments 1, 2 and 3 respectively. For simplicity reasons, we admit that both walls have identical deflections, i.e. have a total of 12 resulting integration constants which are found from the kinematic, geometric and dynamic boundary/transition conditions. For these we use the relations at Eqs. (37) and (38) which link derivatives of the deflection function $u(y)$ and the bending moment $M_B(y)$ resp. transversal force $Q(y)$,

$$M_B(y) = q\frac{\partial^2 u(y)}{\partial y^2}, \tag{37}$$

$$Q(y) = -\frac{\partial^2 M_B(y)}{\partial y} = -q\frac{\partial^3 u(y)}{\partial y^3} \tag{38}$$

where

$$q = EI_z \tag{39}$$

quantifies the structure local rigidity. Indexed rigidity factors q_i used hereafter refer to the values of each of the segments 1 to 3.

Equating the deflections, slopes, bending moments and transversal forces yields in $y = 0$

$$u_1(0) = \frac{\partial u_1(0)}{\partial y} = 0 \tag{40}$$

In $y = l_1$ we get

$$u_1(l_1) = u_2(l_1), \tag{41}$$

$$\frac{\partial u_1(l_1)}{\partial y} = \frac{\partial u_2(l_1)}{\partial y}, \tag{42}$$

$$q_1\frac{\partial^2 u_1(l_1)}{\partial y^2} = q_2\frac{\partial^2 u_2(l_1)}{\partial y^2}, \tag{43}$$

$$q_1\frac{\partial^3 u_1(l_1)}{\partial y^3} = q_2\frac{\partial^3 u_2(l_1)}{\partial y^3}, \tag{44}$$

In $y = l_1 + l_2$:

$$u_2(l_1 + l_2) = u_3(l_1 + l_2), \tag{45}$$

$$\frac{\partial u_2(l_1 + l_2)}{\partial y} = \frac{\partial u_3(l_1 + l_2)}{\partial y}, \tag{46}$$

$$q_2\frac{\partial^2 u_2(l_1 + l_2)}{\partial y^2} = q_1\frac{\partial^2 u_3(l_1 + l_2)}{\partial y^2}, \tag{47}$$

$$q_2\frac{\partial^3 u_2(l_1 + l_2)}{\partial y^3} = q_1\frac{\partial^3 u_3(l_1 + l_2)}{\partial y^3}. \tag{48}$$

In $y = 2l_1 + l_2$ we have

$$\frac{\partial u_3(2l_1 + l_2)}{\partial y} = 0, \tag{49}$$

as well as dynamic equilibrium between transversal forces in the walls, driving force $\widehat{F}$ and fluid force $\Delta S\widehat{\tau}_{yx}$, i.e.

$$-2\frac{\partial^3 u_3(2l_1 + l_2)}{\partial y^3} + \widehat{F} - \Delta S\widehat{\tau}_{yx} = \omega^2 m_1 u_3(2l_1 + l_2) \tag{50}$$

with $\widehat{X} = u_3(2l_1 + l_2)$ in the definition of $\widehat{\tau}_{yx}$ (Eq. 17). $\widehat{X}$ is obtained by solving the linear equation system at Eqs. (40), (41), (42), (43), (44), (45), (46), (47), (48), (49) and (50) and substituting the integration constants which correspond to the upper part in Eq. (36) with $y = 2l_1 + l_2$. The solution is not explicitly given here for space reasons but is easily found, the system being linear and relatively sparse. The probe transfer function is obtained with Eq. (1). f_{res} and df are then obtained as a function of the fluid rheological properties by solving Eqs. (2) and (3) with the secant method.

Theoretical results and comparison of both models

The models outlined above do not include any freely adjustable parameters. However, the idealizations which had to be made allow some freedom on geometrical parameters like the lateral wall segments length, which can to some extent be adjusted to fit measured values. Since both models are based on different assumptions, the fine adjusting of these geometrical parameters may lead to values which may differ slightly between both models.

We first note that the models are in good accordance with each other in the first fundamental frequency region, up to a horizontal shifting factor on the frequency axis. Indeed, the discrete model yields for identical resonator parameters a resonant frequency which is about 60 Hz higher than the one predicted by the continuous model based on flexural oscillations. This can be qualitatively explained by the fact that the assumed rigidity of the central part in the discrete model is practically identical to an infinite elasticity modulus for this segment, which logically shifts the fundamental frequency towards higher values. Although the fundamental frequency depends on numerous parameters, we choose to horizontally shift the $Arg(G_T^*)$ vs. f curve predicted by the discrete model by modifying only the length l_1 of the compliant lateral wall part, as well as l_2 according to $l_1 + l_2 = l_{tot}$, since the sum is measurable with a smaller margin of error. As mentioned above, l_1 is not a freely adaptable parameter, and a difference between the values used in both models is acceptable only as long as it does not exceed the uncertainty induced by the geometry idealization, like the lack of consideration of the curvature radii at the cross sections transitions. The system parameters used in each model as well as their numerical value for the present experimental set-up are listed in Table 1. These are identical for both models, with the exception of the lateral walls segment lengths l_1 and l_2

which are fitted to the measured fundamental frequency within the limits mentioned above. In the present case, the difference of 0.9 mm which brings both fundamental frequencies to correspond is still essentially smaller than the sum of both curvature radii at the cross sections transitions, which is 3.0 mm. The imaginary part of the probe material elastic given in Table 1 accounts for the resonator intrinsic damping. This value is obtained form the *df* value of the unloaded probe, which equals 0.17 Hz with $\Delta\alpha = 22.5°$ and T = 23 °C.

Figure 4 shows the $\mathrm{Arg}(G_T^*)$ vs. *f* curve which is computed with both models when the resonator is in contact with three Newtonian fluids of 0.1, 1 and 10 Pas confined in a 100-µm gap. Figure 5 shows the *df* value predicted by both models in the vicinity of the fundamental frequency vs the Newtonian viscosity η for different gap widths and $\Delta\alpha = 22.5°$. The accordance between both models is good, with a systematically

higher damping value predicted by the discrete model. This can be qualitatively explained by the larger value for l_1 used in the discrete model, which makes the resonator more compliant, and hence increases its sensitivity.

Experiment

Experimental setup The experimental setup consists of one resonator and one control unit linked to a PC. The control unit incorporates a function generator, a power amplifier, a phase shifter as well as a XOR-gate, as described in Fig. 2.

As stated above, a noticeable feature of the measuring algorithm is the use of one single electromagnetic device for driving and sensing of the resonator. As a consequence, the actual deflection measurement is strictly speaking made in free damped decay, for driving and sensing take place successively. Therefore stationary

Fig. 4 Comparison of $\phi = \mathrm{Arg}(G_T^*)$ obtained with discrete (*dotted line*) and continuous models (*continuous line*) for $d = 100$ µm and (1) $\eta = 0.1$ Pas, (2) $\eta = 0.1$ Pas and (3) $\eta = 10$ Pas
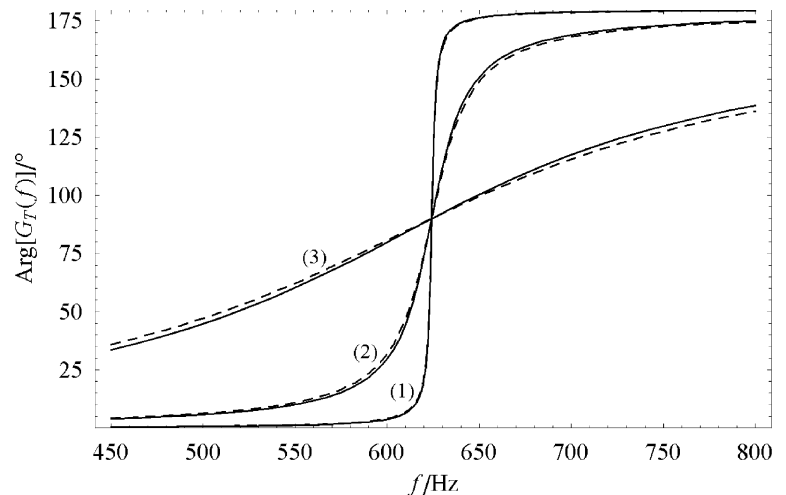

Fig. 5 Comparison of $df(\eta)$ curves for Newtonian fluids obtained with discrete (*dotted lines*) and continuous model (*continuous lines*) for $\Delta\alpha = 22.5°$. The gap width *d* is equal to (1) 50 µm, (2) 100 µm, (3) 200 µm and (4) 2 mm
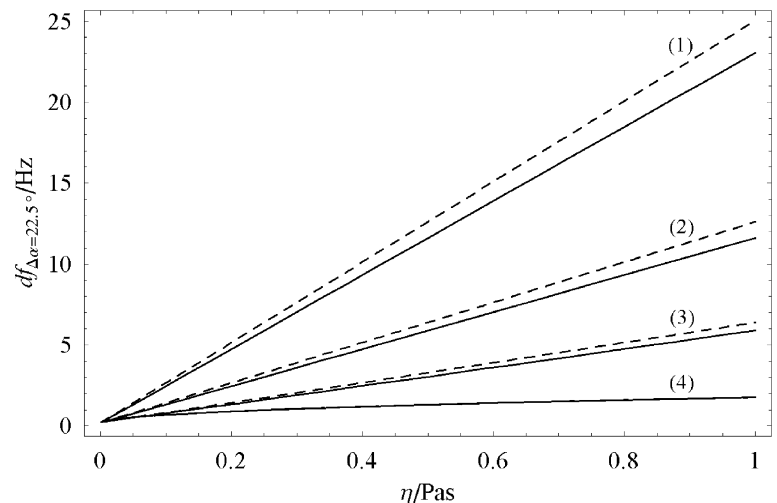
Table 2 Newtonian samples properties

Sample	Composition	Supplier	Product name	η_0/mPas (23°C)	ρ/kg.m^{-3} (23°C)
N1	*n*-Tetradecane 99 + %	Aldrich Chemie		1.81	739
N2	Linear PDMS	Haake	E7	4.07	827
N3	High oleic sunflower oil	Nestlé		74.2	876
N4	Linear PDMS	Wacker	AK10	9.8	968
N5	Polyethylene-glycol	BASF	Pluriol E200	61.0	1120
N6	Polyethylene-glycol	BASF	Pluriol E300	76.1	1125
N7	Polyethylene-glycol	BASF	Pluriol E400	94.2	1128
N8	Linear PDMS	Dow Corning	200	101.2	965
N9	Linear saturated alcanes	Aldrich Chemie	paraffine oil	155	890
N10	PIB/PB copolymer	Infineum	C9945	252	855
N11	Linear PDMS	Wacker	AK100	98.1	972
N12	Linear PDMS	Rhodia Silicones	47V300	292.1	970
N13	Linear PDMS	Dow Corning	200	344.2	970
N14	Linear PDMS	Rhodia Silicones	47V500	472	972
N15	Linear PDMS	Tracomme	670 K	664	974

Table 3 Viscoelastic samples: results of the two-module Maxwell model fit (Eqs. 52 and 53)

Sample	wt% CMC	η_1/Pas	λ_1/s	η_2/Pas	λ_2/s
V1 (*open triangles*)	0.5	0.08	0.78	0.16	0.033
V2 (*open diamonds*)	1.0	0.52	0.48	0.46	0.019
V3 (*filled triangles*)	1.5	2.55	0.51	0.95	0.014
V4 (*filled diamonds*)	2.0	12.1	0.56	2.15	0.013
V5 (*filled circles*)	2.5	40.9	0.76	4.61	0.012
V6 (*filled squares*)	3.0	60.6	0.79	5.73	0.013

measurements of f_{res} and *df* are performed for comparison with the control unit (phase-locked loop) measured values. For this we drive the resonator and fluid system with an external power amplified function generator (Minilab 603, BWD, Australia) and use a laser interferometer (OFV 2100 with OFV 300 laser, Polytec, USA), an oscilloscope (9314 M, LeCroy, USA) and a frequency meter (9921, Racal-Dana, UK) to record the argument of the transfer function in the vicinity of the resonant frequency. This set-up allows a strictly stationary measurement of the resonant dynamical behaviour of the coupled system.

Reference viscosity measurements of the fluid samples are made with a Rheometrics ARES rheometer (Rheometric Scientific, USA), with a 50-mm, 1° cone-plate geometry and 20-mNm torque sensor. Densities are measured with a DMA 4500 Density Meter (Paar Physica, Germany).

Materials The first group of samples is described in Table 2. Most of these fluids are expected to be Newtonian in the context of the present experiment, i.e. their longest relaxation time is expected to be shorter than $(2\pi f_{res})^{-1}$. Hence the viscosity of such fluids as obtained with classical, low frequency rotational viscometers can be expected to be valid at the probe operating frequency of ca. 623 Hz. This allows us to compute the *df* values with the models above and thus to test experimentally the validity of these.

Most of the samples used in this work consist of polydimethyl siloxane (PDMS) melts. According to the work of Hadjistamov (1996), at the probe operating frequency of 623 Hz, entangled PDMS melts with zero shear rate viscosities above ca 500 mPas can be expected to show a viscoelastic character. Since a 500 mPas PDMS melt is only weakly entangled (Longin et al. 1998), this limit can be considered as rather conservative. Nonetheless, the Newtonian character of the most viscous samples of Table 2 cannot be assumed a priori.

Low T measurements were performed on the viscous PDMS samples to verify the Newtonian character at higher frequencies, based on the time temperature superposition principle (Ferry 1980).

These indicate that all samples are Newtonian at 623 Hz, with the precision which typically characterizes the superposition.

The second group of samples consists of fluids which show a non-negligible elastic behaviour even at low frequencies. The sample viscoelastic fluids used here consist of sodium carboxymethyl cellulose (CMC) aqueous solutions. Sodium CMC was provided by Aqualon. The essentially viscoelastic character of the CMC samples can be seen at the relaxation times obtained by fitting a two-module Maxwell model to low-frequency data. The model assumes a complex shear modulus of the form

$$G^*(\omega) = \eta_1 \frac{i\omega}{1 + i\omega\lambda_1} + \eta_2 \frac{i\omega}{1 + i\omega\lambda_2} \tag{51}$$

Storage and loss moduli are accordingly given by

$$G'(\omega) = \eta_1 \frac{\lambda_1\omega^2}{1 + \lambda_1^2\omega^2} + \eta_2 \frac{\lambda_2\omega^2}{1 + \lambda_2^2\omega^2} \tag{52}$$

$$G''(\omega) = \eta_1 \frac{\omega}{1 + \lambda_1^2\omega^2} + \eta_2 \frac{\omega}{1 + \lambda_2^2\omega^2} \tag{53}$$

The viscosities (η_1, η_2) and corresponding relaxation times (λ_1, λ_2) obtained from a log-log least-squares fit of the measured G^* values in the 1–150 rad s^{-1} frequency range are given in Table 3. The viscoelastic character of the CMC solutions is displayed in Figs. 6 and 7.

Results

Newtonian samples

Figure 8 shows the *df* values obtained with sample fluids described in Table 2, together with theoretical values. Measurements were made with three gap settings,

Fig. 6 $|\eta^*|$ vs ω in the 1–150 rad s^{-1} frequency range for the CMC samples of Table 3. *Open triangles*: 0.5 wt%; *open diamonds*: 1.0 wt%; *filled triangles*: 1.5 wt%; *filled diamonds*: 2.0 wt%; *filled circles*: 2.5 wt%; *filled squares*: 3.0 wt%
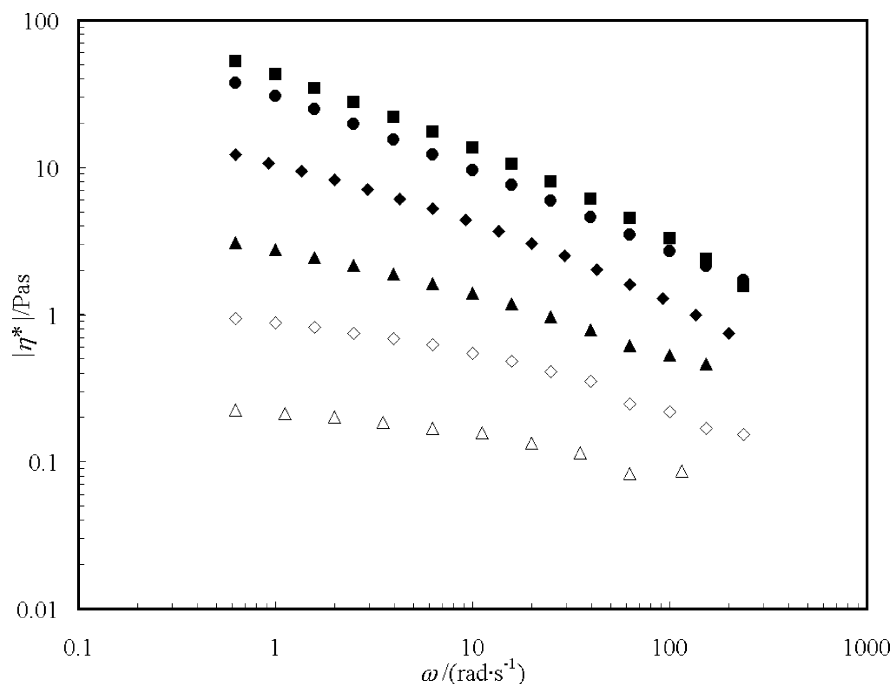

Fig. 7 $\delta = \mathrm{Arctan}(G''/G')$ vs ω in the 1–150 rad s^{-1} frequency range for the CMC samples of Table 3. *Open triangles*: 0.5 wt%; *open diamonds*: 1.0 wt%; *filled triangles*: 1.5 wt%; *filled diamonds*: 2.0 wt%; *filled circles*: 2.5 wt%; *filled squares*: 3.0 wt%
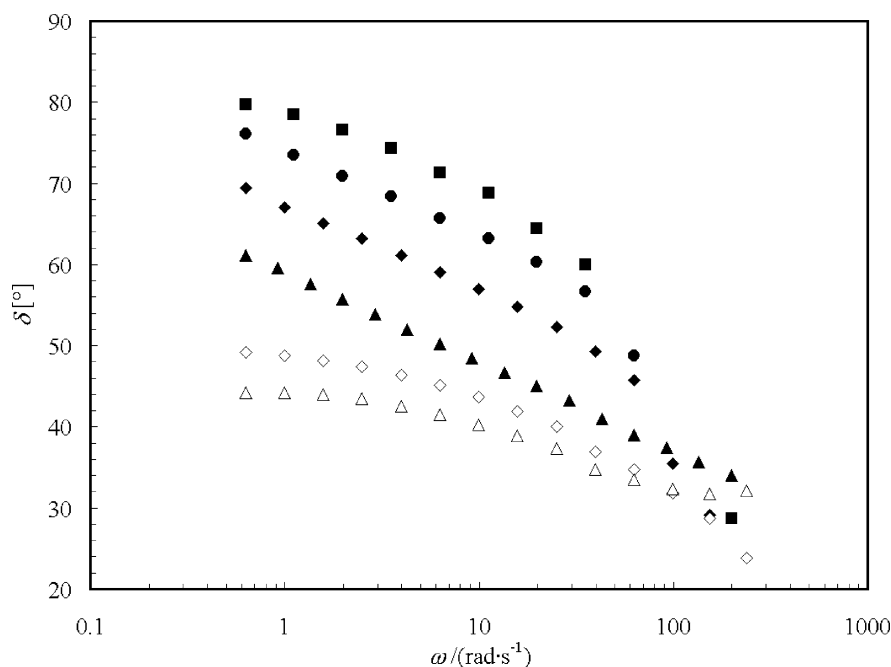

respectively 100, 150 and 200 μm. The dashed lines represent the *df* value predicted by the discrete model, for a fluid with a relative density of 1. Continuous lines represent *df* values computed with the continuous model. Squares represent pseudo-stationary values obtained with the control-unit. Measurements were performed with 12 driving cycles and 3 sensing cycles. Circles represent *df* values obtained by measuring

$\phi = \mathrm{Arg}(G_T^*(f))$ with the laser interferometer in the vicinity of f_{res}, i.e. under stationary conditions. $\Delta\alpha$ was set to 22.5° for all measurements.

For the samples of Table 2, the variation of f_{res} measured with both phase-locked loop control unit as well as the laser interferometer is smaller than the margin of error which affects the measurements. This is in accordance with the theoretical predictions since both

Fig. 8 Theoretical and measured *df* values. *Hollow symbols*: *d* = 100 µm, *grey symbols*: *d* = 150 µm, *dark symbols*: *d* = 200 µm. *Squares*: values obtained with the control-unit (pseudo-stationary conditions). *Circles*: values obtained with the laser interferometer (stationary conditions). *Continuous lines*: values predicted by the continuous model. *Dashed lines*: values predicted by the discrete model. Right-hand axis: corresponding *Q* factor, Eq. (54)
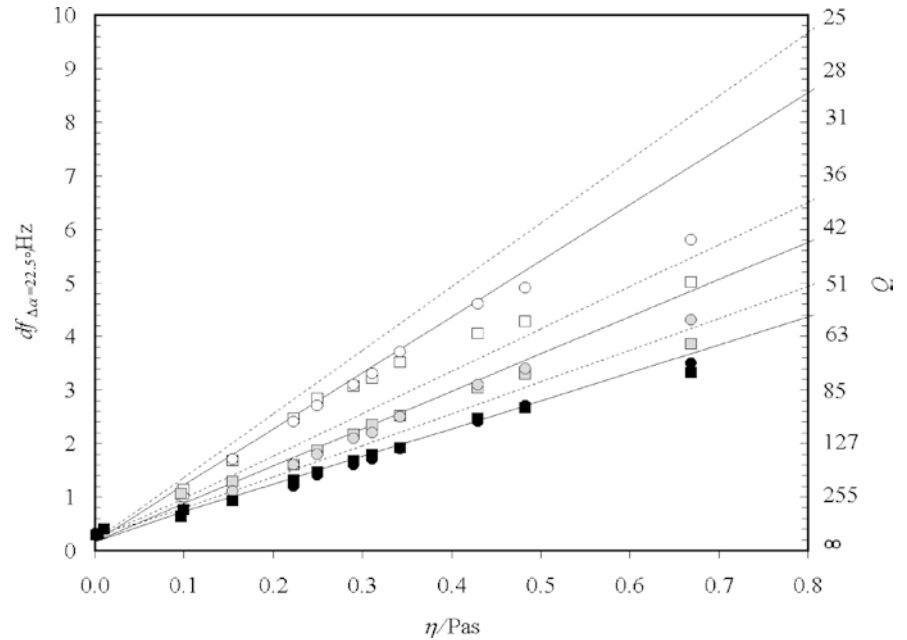
models predict with a variation of less than 0.2 Hz over the investigated viscosity range. This is caused by the fact the so-called gap loading condition (Schrag 1977) $d < \delta$ is fulfilled in most cases, so that a decrease of f_{res} as a consequence of the mass loading inherent to an increase of δ is inhibited by the finite gap thickness.

Viscoelastic samples

Qualitatively, the influence of a viscoelastic fluid on the resonant frequency of the system is twofold. On one hand, the elastic character tends to shift the resonant frequency towards higher values, for it increases the system stiffness. On the other hand, the fluid increases the mass of the oscillating system, thus shifting the resonant frequency to smaller values. This latter aspect is limited by the finite gap thickness if $d < \delta$ as mentioned above. In contrast to Newtonian fluids (which induce almost no change in f_{res}, because they show no elastic response and the sample is fully gap loaded), the elastic response of a viscoelastic fluid contributes to the increase of resonant frequency, especially in the gap loading case. We are hence in principle able to measure both viscosity and elasticity of the fluid in terms of complex viscosity $\eta^* = \eta' - i\eta''$ or complex shear modulus $G^* = i\omega\eta^*$ from damping *df* and the f_{res} shift.

Measurement results for viscoelastic fluids cannot be presented as in Fig. 8, for the fluid cannot be characterized through one single parameter like the zero shear rate viscosity η_0 for Newtonian fluids. Considering Fig. 6, we expect for instance the measured damping

values of the viscoelastic samples to be small, given the trend observed in the frequency range reachable with the rotational rheometer. In Table 4 we show the measured f_{res} and *df* values for the viscoelastic samples listed in Table 3, together with complex viscosity values obtained from inversion of the discrete model. Numerical inversion of the continuous model yields close values, but is extremely time consuming. Pseudo-stationary values measured with the control unit agree here with the stationary, laser interferometer measured ones, as expected for low dampings (Romoscanu 2003).

Discussion

Newtonian samples

As one can see from Fig. 8, good accordance between continuous model computed and laser interferometer measured *df* values is observed over the whole investigated viscosity range. In contrast, values measured directly with the control unit (i.e. under pseudo-stationary conditions) correspond to computed and laser interferometer measured ones only up to a *df* value of about 3 Hz, above which the first are smaller. In terms of mechanical quality factor *Q* (Sayir 1994),

$$Q = \frac{f_{res}}{df_{\Delta\alpha=45°}} \cong \frac{f_{res}}{df_{\Delta\alpha}} \tan(\Delta\alpha) \qquad (54)$$

this represents, with $f_{res} \cong 623$ Hz and $\Delta\alpha = 22.5°$, a minimum factor $Q_{min} \cong 86$ (to be compared to the unloaded probe factor $Q_0 \cong (623/0.17)\tan(22.5°) \cong 1500$). Above this value, results obtained with the pseudo-stationary

Table 4 Measured f_{res} and df values for viscoelastic samples. PS = values measured with the control unit; LI = values measured with the laser interferometer. η' and η'' obtained from numerical inversion the discrete model

Sample	f_{res}/Hz(PS)	df/Hz(PS)	f_{res}/Hz(LI)	df/Hz(LI)	γ/%	η'/mPas	η''/mPas	δ/°	$\lvert\eta^*\rvert$ /mPas
No fluid	622.80	0.16	622.8 ± 0.2	0.16	–	–	–	–	–
V1 (*open triangles*)	623.13	0.39	623.1 ± 0.2	0.4	3.5	18	30	31	35
V2 (*open diamonds*)	623.53	0.47	623.6 ± 0.2	0.5	2.5	25	59	23	64
V3 (*filled triangles*)	624.13	0.60	624.2 ± 0.2	0.6	2.1	36	103	19	109
V4 (*filled diamonds*)	624.56	0.81	624.6 ± 0.2	0.8	1.7	55	134	22	145
V5 (*filled circles*)	625.04	1.01	625.1 ± 0.2	1.1	1.5	72	169	23	184
V6 (*filled squares*)	625.63	1.09	625.8 ± 0.2	1.1	1.4	79	211	21	225

algorithm which is implemented in the control unit corroborate strictly stationary laser interferometer results. At lower Q factors, pseudo-stationary df values are smaller than the laser interferometer and computed ones. We conclude that in the $\lvert\eta^*\rvert \leq 670$ mPas range, the discrepancy has a mainly instrumental, and not rheological, origin. In other words, the smaller pseudo-stationary values are due to an measurement algorithm artefact rather than to a viscoelastic sample behaviour (typically characterized by a decrease of $\lvert\eta^*\rvert$ with increasing frequency as in Fig. 6). This can also be seen without considering the stationary laser interferometer measurements, from results obtained with the pseudo-stationary algorithm only, provided such measurements are performed at different gap widths d. If the discrepancy had a rheological origin, it would be observed for all $\lvert\eta^*\rvert$ exceeding a given, gap-independent value[1]. In the present case, one can see as stated above that discrepancy occurs systematically above a fixed $df \cong 3$ Hz. This damping value is reached at $\lvert\eta^*\rvert$ values which increase with increasing gap. In the measurements made with the smallest d value (and thus lowest Q values) pseudo-stationary values begin to differ from stationary ones at a $\lvert\eta^*\rvert$ value of ca 0.3 Pas. However PDMS melts with this viscosity should behave as Newtonian fluids at $f = f_{res}$ (Hadjistamov 1996). Consequently, the discrepancy between pseudo-stationary values and model/stationary values observed at $df > 3$ Hz ($Q < Q_{min} \cong 86$) must be due to a measurement artefact. We note that Emphasis Type = "Italic" > Q_{min} values of the same order as the value observed here are observed with other geometries and at essentially different frequencies when the same pseudo-stationary measurement algorithm is used (Romoscanu 2003).

A comprehensive discussion of the influence of the pseudo-stationary algorithm shown in Fig. 2 on the probe raw data is outside the scope of this paper. Such a discussion can be found in Romoscanu (2003), where a method for the correction of the probe raw data at low Q values, i.e. when the artefact cannot be neglected, is also proposed. The interest of such a correction (which would allow the use of the pseudo-stationary algorithm at $Q < Q_{min}$) is obvious since the use of a laser as part of the experimental setup cannot be considered as a valid alternative to the pseudo-stationary algorithm in an applied use of the resonator. As far as simplicity, cost-effectiveness and convenience are concerned, both methods cannot be compared.

Viscoelastic samples

Figure 6 shows that, for the viscoelastic samples measured here, $\lvert\eta^*\rvert$ decreases by around one order of magnitude in the 1–150 rad s^{-1} range. From this point of view, the high frequency results shown in Table 4 are consistent. This is shown in Fig. 9 and Table 5 where the measured low frequency $\lvert\eta^*\rvert$ values are extrapolated (dotted lines) to f_{res} using the power law model at Eq. (55). The parameters a and b are obtained from a least square fit of the low-frequency data, based on the approximately constant slope in the log-log graph, Fig. 6. As pointed out by Larson (1999), the viscosity of dilute polymers has a theoretical high-frequency limit which is of the order of magnitude of the solvent viscosity η_s. The results shown in Table 5 show that the operating frequency of the probe used here, ca 0.6 kHz, is obviously still significantly lower than the high frequency limit.

$$\lvert\eta^*\rvert = b\omega^a \tag{55}$$

Experimental values of $\delta < 45°$ ($\eta'' > \eta'$) are also consequent with the low-frequency values shown in Fig. 7. Quantitatively, η'' measurements are reproducible with a margin of error of ca. 20%, a value which is larger than for η' measurements, and which will also affect $\lvert\eta^*\rvert$ and δ. Some sources of error which are typical for aqueous solutions may partially be responsible for this. For instance, the sample visibly shrinks on a time scale which is larger than the measuring time (many minutes compared to seconds), as one can observe through the upper, transparent fixed plate. This can for instance have an influence on the reproducibility of the measurements, especially if solvent evaporation or concentration changes occur in the vicinity of the sample lateral surface. Measurements with variation of the

---

[1] As long as the gap is large enough for the sample to be considered as a continuum.

Fig. 9 Extrapolation of low frequency $|\eta^*|$ data to $f_{res} \cong 623$ Hz and comparison with experimentally determined values. *Open triangles*: 0.5 wt%; *open diamonds*: 1.0 wt%; *filled triangles*: 1.5 wt%; *filled diamonds*: 2.0 wt%; *filled circles*: 2.5 wt%; *filled squares*: 3.0 wt%
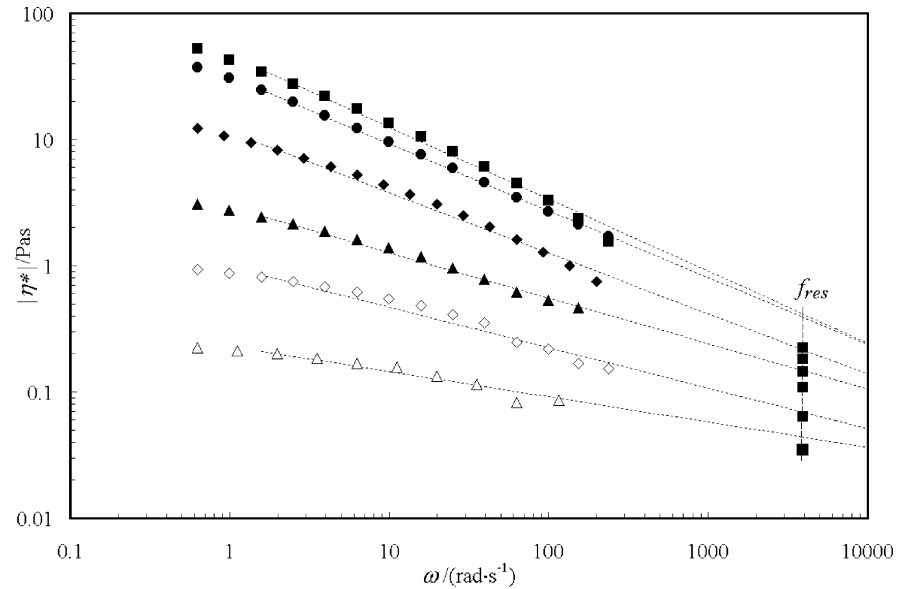

Table 5 Extrapolation of low frequency $|\eta^*|$ data to $f_{res} \cong 623$ Hz and comparison with measured values

Sample	$|\eta^*| = b\omega^a$ (model)		$|\eta^*|$/mPas from extrapolation to $f_{res} \cong 626$ Hz	Resonator measured $|\eta^*|$/mPas
	a	b		
V1 (*open triangles*)	−0.20	0.23	43	35
V2 (*open diamonds*)	−0.32	0.98	72	64
V3 (*filled triangles*)	−0.36	2.91	152	109
V4 (*filled diamonds*)	−0.48	11.48	222	145
V5 (*filled circles*)	−0.53	31.38	399	184
V6 (*filled squares*)	−0.57	46.54	394	225

fluid/plates wettability have not been done yet but should be performed in the future.

Conclusion

In the previous sections it is shown that the resonating device behaves in a wide extent according to the idealized theoretical models. Among both proposed models, the continuous one based on flexural oscillations of the resonator lateral walls yields theoretical values which are closer to the measured ones. This model is however not appropriate in its actual form for a concrete implementation in the resonator control unit software because of the much more complicated numerical inversion procedure. Since both models rely to some extent on an idealization of the actual geometry, the introduction of a correction factor in the discrete model can be justified.

One of the essential features of the present instrument is the pseudo-stationary phase-shift based method, with successive driving and sensing of the probe performed by a single electromagnetic device. The results presented above show that the method can be used to build a particularly simple and inexpensive rheometric device. The limitation resides in minimum system Q factor. Indeed, the algorithm underestimates the measured damping in an extent which depends on the system Q factor. For $Q < Q_{min} \cong 86$ (a value which is reached at $|\eta^*|$ values of a few hundred mPas with usual gap widths, due to the almost linear relationship between df and $|\eta^*|$ under gap loading) pseudo-stationary probe raw data need to be corrected before inversion of the model is made, if strictly stationary laser interferometer measurements are not considered as an option. This can be done by converting the biased control unit measured values into the true stationary values, with the help of a calibrated relationship based on stationary laser interferometer measurements. This solution has an important drawback, namely that it would imply a partially calibrated implementation of the instrument. Alternatively, the effects of the pseudo-stationary algorithm can be corrected by modelling the influence of the used algorithm on measured probe raw data f_{res} and df. Such an approach, which can be found in Romoscanu (2003), is outside the scope of this paper. It must be noted that the value of $Q_{min} \cong 86$ observed here is significantly lower than the unloaded probe factor $Q_0 \cong 1500$, so that the

above-mentioned artefacts are quantitatively relevant only at relatively large system dampings.

On the other hand, if $Q > Q_{min}$, the error induced by the algorithm is quantitatively negligible, i.e. not larger than other usual experimental sources of error. In this case, the fluid complex viscosity can be inferred from uncorrected pseudo-stationary probe raw data. Provided this condition is fulfilled (as for the CMC solutions above), the experimental setup described above can be considered as a simple and efficient tool for the measurement of high frequency fluid rheological properties.

References

Bird RB, Armstrong RC, Hassager O (1987) Dynamics of polymeric liquids, 2nd edn, vol 1. Wiley

Birnboim NH, Elyash LJ (1966) Dynamic mechanical properties of dilute polymer solutions. Bull Am Phys Soc Ser 11:165–166

Blom C, Mellema J (1984) Torsional pendula with electromagnetic drive and detection system for measuring the complex shear modulus of liquids in the frequency range 80–2500 Hz. Rheol Acta 23:98–105

Ferry JD (1980) Viscoelastic properties of polymers, 3rd edn. Wiley

Glover GM, Hall G, Matheson AJ, Stretton JL (1968) A magnetostrictive instrument for measuring the viscoelastic properties of liquids in the frequency range 20–100 kHz. J Sci Instr J Phys E 1:383–388

Hadjistamov D (1996) Oscillatory measurements on silicone oils—loss and storage modulus master curves. Rheol Acta 35:364–368

Kirschenmann L, Pechhold, W (2002) Piezoelectric rotary vibrator (PRV)—a new oscillating rheometer for linear viscoelasticity. Rheol Acta 41:362–368

Landau LD, Lifshitz EM (1994) Physique théorique-mécanique des fluides, 3rd edn. Mir-Ellipses. ISBN 2-7298-9423-3

Larson RG (1999) The structure and rheology of complex fluids. Oxford University Press

Longin PY, Verdier C, Piau M (1998) Dynamic shear rheology of high molecular weight PDMS: comparison of rheometry and ultrasound. J Non-Newtonian Fluid Mech 76:213–232

Mason WP (1947) Measurement of the viscosity and shear elasticity of liquids by means of a torsionally vibrating crystal. Trans ASME 39:359–370

Romoscanu AI (2003) High frequency rheometry on homogeneous and heterogeneous fluids. PhD Thesis. ETH Zurich

Sayir MB (1994) Mechanik 3. ETH Zurich

Sayir M, Goodbread J, Häusler K, Dual J (1995) Method and device for measuring the characteristics of an oscillating system. Patent Corporation Treaty, International Application Number PCT/EP95/00761

Schrag JL (1977) Deviation of velocity gradient profiles from the "gap loading" and "surface loading" limits in dynamic simple shear experiments. Trans Soc Rheol 21:399–413

Schrag JL, Johnson RM (1971) Application of the Birnboim multiple lumped resonator principle to viscoelastic measurements of dilute macromolecular solutions. Rev Sci Instr 42:224–232

Stokich TM, Radtke DR, White CC, Schrag JL (1994) An instrument for the precise measurement of low viscosity dilute macromolecular solutions at frequencies from 20 to 500 kHz. J Rheol 38:1195–1210

Tanner RI (2000) Engineering rheology, 2nd edn. Oxford University Press